Ab Initio Based Double-Sheeted DMBE Potential Energy Surface for N-3((2)A '') and Exploratory Dynamics Calculations

2 AUTHORS:

Breno Galvão
Centro Federal de Educação Tecnológica de …
16 PUBLICATIONS   73 CITATIONS

SEE PROFILE

Antonio J. C. Varandas
University of Coimbra
382 PUBLICATIONS   6,733 CITATIONS

SEE PROFILE

Ab Initio Based Double-Sheeted DMBE Potential Energy Surface for N$_3$($^2A''$) and Exploratory Dynamics Calculations

B. R. L. Galvão and A. J. C. Varandas*

Departamento de Quimica, Universidade de Coimbra, 3004-535 Coimbra, Portugal

ⓈSupporting Information

ABSTRACT: We report a global accurate double-sheeted potential energy surface for the lowest doublet states with $^2A''$ symmetry of the N$_3$ radical using the double many-body expansion method. The functional form ensures by construction the degeneracy of the two adiabatic sheets along the D_{3h} line and the corresponding cusp behavior. Calibrated from multireference configuration interaction energies, it reproduces all the predicted stationary structures on both sheets and ensures a correct description of the dissociation limits. A test quasiclassical trajectory study of N(^2D) + N$_2$ collisions is also reported in the lowest adiabatic sheet of the potential energy surface. The results commend it for both classical and quantum dynamics studies, while serving as a building block for the potential energy surfaces of larger nitrogen allotropes and azides.

1. INTRODUCTION

New allotropes of nitrogen have been recently much studied,[1,2] because they stand as good candidates for high energy and density materials. For such studies, a deep understanding of its simplest trimeric form (N$_3$) is of fundamental importance. In fact, it may play a role on intermediate reactions, and has been suggested as a starting material for building larger polynitrogenic structures such as N$_4$(T_d).[3] The unstable quartet state of N$_3$ has recently been studied in our group[4,5] due to the importance of N(^4S) + N$_2$ collisions on designing spacecraft heat shields. In this work, we focus on the bound trinitrogen doublet state, which is of key importance for studying the N(^2D) + N$_2$ reaction either in solid matrices or in atmospheric collisions. Although such collisions have been much studied experimentally,[6–13] no theoretical work regarding its dynamics has thus far been performed.

The N$_3$($^2A''$) ground-state potential energy surface (PES) is known experimentally[14–16] to have a linear minimum ($^2\Pi_g$), while a ring isomer[17] of B_1 symmetry has found support on experimental evidence.[18–23] Ab initio calculations[24] confirmed this isomer to be stable with respect to both spin-allowed and spin-forbidden decomposition and separated from the linear minima by a barrier of 33 kcal mol^{-1}. Moreover, its stability in reactions with several atmospheric compounds has been a matter of theoretical investigation.[25,26] The stationary structures of six PESs (two of $^2A''$ symmetry, three $^2A'$, and one $^4A''$) have been much studied by Morokuma and co-workers,[24,27,28] and previously by other groups[3,17,29,30] for geometry optimizations, fundamental frequencies, dipole moments, and minima of crossing seams (MSX).

The linear form of the azide radical (N$_3$) can be formed on solid molecular nitrogen under intense radiation fields that can break the nitrogen triple bond, with such conditions being known to abund in various low-temperature interstellar and solar system environments such as Triton (Neptune's largest moon) and Pluto.[13] In fact, Hudson and Moore[11] have proposed the use of linear N$_3$ as a tracer to follow the abundance of molecular nitrogen in space. The reaction of N$_3$ formation in solid nitrogen has been considered in many experimental studies at low temperature (10−35 K),[6–13] but no evidence of both the cyclic isomer and cyclic/linear reaction pathway has been found, although the cyclic form can be theoretically expected under high energy collisions.[24]

Although the linear isomer is only slightly endoergic relatively to N(^4S) + N$_2$,[31] large barriers caused by the spin-forbidden nature of this process are predicted,[24] and hence, this reaction is unlikely to form the azide radical.[12] On the other hand, the formation of N$_3$ from N(^2D) + N$_2$ collisions is predicted to be highly exothermic while showing small reaction barriers (3 kcal mol^{-1} for the linear isomer and 7 kcal mol^{-1} for the cyclic one[24]). Such collisions should also be interesting for studies of the atmosphere because this excited state of atomic nitrogen is copiously formed in the ionosphere via dissociative recombination of NO$^+$ and N$_2^+$.[32] Moreover, N(^2D) can be generated under experimental conditions via quenching of N$_2$($\tilde{A}^3\Sigma_u^+$) by N(^4S) atoms.[3,33−36]

For accurate studies of reaction dynamics of the above processes, it is mandatory to have a PES, desirably in analytic form, capable of describing the dissociative limits, barriers on the entrance channel and valence regions, and other relevant

topological attributes. Note that the energy necessary to dissociate the system is similar to the isomerization barrier, and hence, the two processes can compete. As a result, any rigorous study of ring closing dynamics should allow for unimolecular decomposition. Analytical representations of the adiabatic PESs proposed thus far for the quartet state have the correct dissociation behavior because their main interest has been on the $N(^4S)$ + N_2 exchange reaction.[4,5,37,38] Conversely, the PESs for the doublet states have been mostly targeted to understand the vibrational spectra of the ring isomer, and hence, only local forms for the latter have thus far been reported.[39−41] More recently, interest arose on ring-closing dynamics studies,[28] with fits of an extended region of configurational space (including cyclic and linear regions) being proposed for two $^2A''$ and three $^2A'$ electronic states. Yet, none of such fits describes the barriers to dissociation and the correct dissociative behavior.

The aim of the present work is to provide the first global analytical representation of the $^2A''$ states of the azide radical, which describes all topological details of the two lowest sheets using double many-body expansion (DMBE)[42−45] theory for the modeling. In particular, a view close to the one adopted for the triplet state of H_3^+ will be adopted.[46] Such a PES should then be useful both for reaction dynamics and for ro-vibrational calculations of the spectra up to the continuum (possibly requiring some further work for enhanced accuracy). Moreover, it may be utilized as a building block for the PESs of larger nitrogen allotropes. The paper is organized as follows. Section 2 contains a summary of the doublet electronic sheets and the details of the ab initio methods employed in this work. The modeling of the PES is described in section 3, while section 4 gathers the main results. A quasiclassical trajectory study performed for the $N(^2D)$ + N_2 reaction is presented on section 5. The conclusions are in section 6.

2. AB INITIO CALCULATIONS AND STATIONARY STRUCTURES

Although this work is concerned only with states of $^2A''$ symmetry, a brief summary of the intricate behavior of other electronic sheets is shown for C_{2v} configurations. The five electronic states that correlate with the $N(^2D)$ + N_2 dissociation limit are considered, namely, 1^2A_2, 1^2B_1, 1^2B_2, 1^2A_1, and 2^2A_2. Note that three other states (2^2B_2, 2^2A_1, and 2^2B_1) exist that correlate with $N(^2P)$ + N_2, but these are of no concern here. They lie higher in energy and show a large number of crossings between themselves and with the quartet state ones. Because such states are repulsive in character, they are not expected to make an important contribution in atom + diatom reaction dynamics.

Calculations at the CASSCF (complete active space self-consistent field) level of theory have first been performed for a grid of values of the $\angle$NNN angle, fixing a C_{2v} symmetry and optimizing the bond length. Note that, for an acute $\angle$NNN angle, the optimization leads to the dissociation limit, as the lowest energy corresponds to very large bond lengths. The results are shown in Figure 1, which allows a simple visualization of almost all the important features for both states that correlate with $^2A''$ in C_s symmetry ($^2B_1$ and $^2A_2$) and also the ones corresponding to $^2A'$ ($^2B_2$ and $^2A_1$), shown in gray. These probing CASSCF calculations show qualitative agreement with previous ones based on higher levels of theory[27] that have been utilized for the location of the stationary structures and crossings (including $^2A'/^2A''$).
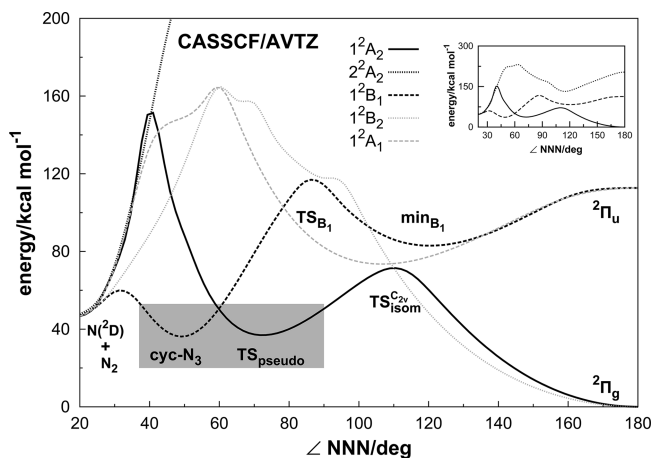
Figure 1. Optimized C_{2v} energy profile, as obtained via CASSCF/AVTZ optimizations at a grid of fixed angles. The electronic states correlating with $^2A''$ are shown in black and the stationary structures assigned, while the ones correlating with $^2A'$ are in gray. Shown by the shaded area are the three important structures associated with cyclic trinitrogen. The insert shows the behavior of the second $^2A_2$ state.

As shown, the azide radical has its deepest minimum at linear geometries, yielding a $^2\Pi_g$ electronic state which is doubly degenerate and correlates with $1^2A'$ and $1^2A''$ in C_s symmetry. In turn, the upper sheet yields a $^2\Pi_u$ structure with two imaginary degenerate bending modes and subject to Renner-Teller deformation via a split into the $2^2A'$ and $2^2A''$ electronic states. The $^2A'$ states will not be fitted in the present work but Figure 1 illustrates an overview of its topology. They are seen to lie high in energy and showing mostly a repulsive behavior for bent geometries. In fact, the most significant detail appears to be the intersection at (or near) a D_{3h} configuration where the $^2A_1$ and $^2B_2$ states become degenerate to form an $^2E'$ state. Distortion of this structure forms a minimum (on the bending coordinate only) of $^2A_1$ symmetry, which is also a result from the Renner−Teller stabilization of the $^2\Pi_u$ structure. While the $^2B_2$ state shows a rather complicated behavior caused by crossings with a third state of $^2A'$ symmetry, it does not form any low lying stable structure, except the $^2\Pi_g$ minimum. Because the present work focuses on the first two $^2A''$ states ($^2B_1$ and $^2A_2$), which hold the cyclic and linear isomers, the following discussion will be restricted to such states.

Starting from a linear symmetrical configuration and reducing the symmetry to C_{2v} by bending, the $^2A_2$ ground state passes through an isomerization barrier (which looks like a transition state in the reduced dimensionality of the plot, and is shortly denoted for later reference as $TS_{isom}^{C_{2v}}$), while the $^2B_1$ upper state shows a local minimum (min_{B_1}) and, subsequently, a transition state (TS_{B_1}); a new transition state connecting min_{B_1} with the $N(^2D)$ + N_2 dissociation channel has also been found and will be described later. At the D_{3h} configuration, that is, $\angle$NNN = 60°, both states become degenerate at the conical intersection of $^2E''$ symmetry, which then distorts to form two ring structures, the cyclic isomer (cyc-N_3) and the transition state for pseudorotation (TS_{pseudo}). Because the two structures lie close in energy, the pseudorotation motion is almost barrier-free,[39,40] with the vibrational wave function spanning both the cyc-N_3 and TS_{pseudo} regions. Figure 1 also shows that, for a T-shaped path, the dissociation on the ground state has a small barrier, while the upper presents a complicated behavior due to the approach of the second state of $^2A_2$ symmetry. This (2^2A_2) lies much higher in
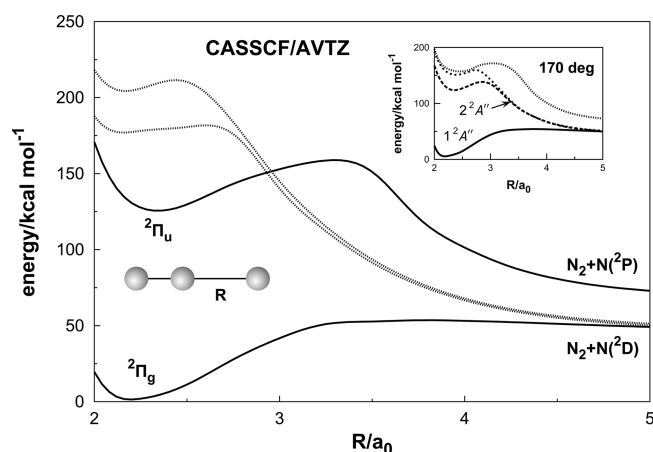
Figure 2. Linear dissociation obtained via CASSCF/AVTZ calculations for $^2A''$ states at a grid of values of one bond length, with the other relaxed. The insert shows the dissociation at a value of $\angle$NNN fixed at 170°.

energy, showing (see inset) a bent minimum that corresponds to a highly energetic form of N_3.

Because Figure 1 is restricted to C_{2v} geometries, it hides the fact that $TS_{isom}^{C_{2v}}$ is actually a second-order saddle point where the antisymmetric stretching mode leads to the real isomerization transition state ($TS_{isom}^{C_s}$), although both forms lie energetically close to each other (within 1 kcal mol^{-1}). Another feature that could not obviously be shown in such a C_{2v} cut refers to linear dissociation, which is shown in Figure 2 for the A'' states. Note that, although the $^2\Pi_u$ state would dissociate to N(^2P) + N$_2$, the crossing with a third state makes the $2^2A''$ sheet dissociate instead to N(^2D) + N$_2$ for all other bond angles, as show in the inset for $\angle$NNN = 170°.

To model the DMBE function, we have performed multi-reference configuration interaction calculations, including the Davidson correction, MRCI(Q),[47,48] with the MOLPRO package[49] and AVTZ[50,51] basis set. Unfortunately, the state-averaged calculations for the two lower states of $^2A''$ symmetry have shown severe difficulties to converge for large atom–diatom separations, as both states become degenerate at this asymptote, and hence, they cannot describe the barriers on the entrance channel that are crucial in reactive dynamics. To overcome such a problem, we have also performed single-state calculations on the lower sheet that cover this region. Although such single-state calculations yield results that differ slightly from the state-averaged ones, the differences involved are rather small (with a root-mean-squared error of ∼0.2 kcal mol^{-1} at the critical regions near the conical intersections and at a set of randomly chosen geometries). Because this deviation is expected to be smaller than the errors due to the fitting procedure and even the expected accuracy of the ab initio methodology itself, we have also used such single-state calculations on the fit of the lower sheet.

We have tested the accuracy of the MRCI(Q)/AVTZ energies by performing single point calculations with the AVQZ basis followed by extrapolation to the complete basis set limit (CBS). Although AVQZ geometry optimizations for all the stationary structures would be desirable, we have checked that the energy of cyc-N_3 relative to the linear minimum calculated on optimized AVQZ geometries differs only by 0.003 kcal mol^{-1} when compared with the result calculated at the corresponding AVTZ geometries, and hence, the very demanding AVQZ optimizations can be safely avoided.

Table 1. Stationary Structures on the Lower Sheet of $N_3(1^2A'')$ [a]

structure	property	MRCI(Q)			Fitted	
		AVTZ[b]	AVQZ[c]	CBS[c]	ref 28	DMBE
$^2\Pi_g$	R/a_0	2.24			2.24	2.24
	θ/deg	180			180	180
	ΔV	0.0	0.0	0.0	−0.7	0.0
cyc-N_3	R/a_0	2.77			2.86	2.77
	θ/deg	49.8			47.0	50.0
	ΔV	32.2	32.9	33.3	32.2	32.3
TS_{pseudo}	R/a_0	2.47			2.47	2.47
	θ/deg	71.9			72.0	71.8
	ΔV	33.1	33.7	34.1	35.6	33.2
MSX	R/a_0	2.59			2.59	2.59
	θ/deg	60.0			60.0	60.0
	ΔV	45.4			45.0	45.0
$TS_{isom}^{C_s}$	R_1/a_0	2.31				2.26
	R_2/a_0	2.62				2.70
	θ/deg	109				109
	ΔV	65.0	66.4	67.4		65.1
$TS_{isom}^{C_{2v}}$ [d]	R/a_0	2.44			2.43	2.44
	θ/deg	109			106	108
	ΔV	66.1	67.4	68.3	62.7	65.7
$TS_{diss}^{C_{\infty v}}$	R_1/a_0	4.23				4.19
	R_2/a_0	2.09				2.09
	θ/deg	180				180
	ΔV	61.8	63.2	64.2		61.8
$TS_{diss}^{C_{2v}}$	R/a_0	4.23				4.16
	θ/deg	28.9				29.4
	ΔV	65.7	67.3	68.3		65.8
$TS_{diss}^{C_s}$ [d]	R_1/a_0					2.12
	R_2/a_0					3.49
	θ/deg					106
	ΔV					69.3
N(^2D)+N$_2$	ΔV	59.0	60.4	61.4		59.0

[a] Energies are given in kcal mol^{-1} relative to the ground $\tilde{X}^2\Pi_g$ state. [b] From ref 24. [c] At the geometries of column 3. [d] Second-order saddle point.

As usual, the CBS extrapolations will be carried out in split form by treating separately the CASSCF and dynamical correlation components of the energy as obtained with Dunning's AVXZ basis set.[50,51] For the CASSCF energy calculated with $X = T,Q$, the most convenient scheme is perhaps the one due to Karton–Martin[52] (although originally suggested for the Hartree–Fock energy, it has been shown[53] to perform well also for the CAS energy since it does not include any dynamical correlation). Similarly, the dynamical correlation can be reliably extrapolated by using the USTE(T,Q)[53] protocol. Thus, the extrapolated CBS limit of the CAS energy has been calculated by fitting the energies with $E_X^{CAS}(\mathbf{R}) = E_\infty^{CAS}(\mathbf{R}) + B/X^{5.34}$, while the dynamical correlation (E_∞^{dc}) was obtained via a fit to

$$E_X^{dc} = E_\infty^{dc} + \frac{A_3}{(X+\alpha)^3} + \frac{A_5(0) + cA_3^{5/4}}{(X+\alpha)^5} \tag{1}$$

12392

dx.doi.org/10.1021/jp2073396 |*J. Phys. Chem. A* 2011, 115, 12390–12398

Table 2. Stationary Structures on the Upper Sheet of $N_3(2^2A'')^a$

feature	property	MRCI(Q)			Fitted	
		$AVTZ^b$	$AVQZ^c$	CBS^c	ref 28	DMBE
$^2\Pi_u$	R/a_0	2.41			2.41	2.40
	$\theta/\deg$	180			180	180
	ΔV	104	106	107	107	105
$\min_{B_1}$	R/a_0	2.39			2.37	2.38
	$\theta/\deg$	120			124	122
	ΔV	72.8	73.5	74.0	70.7	72.9
TS_{B_1}	R/a_0	2.57			2.54	2.55
	$\theta/\deg$	86.1			86.4	85.3
	ΔV	109	111	112	104	108
TS_{C_s}	R_1/a_0					3.04
	R_2/a_0					2.17
	$\theta/\deg$					119
	ΔV					79.8

^{a} Energies are given in kcal mol^{-1} relative to the ground $\tilde{X}^2\Pi_g$ state. ^{b} From ref 28. ^{c} At the geometries of column 3.

where $A_5(0) = 0.0037685459E_h$, $c = -1.17847713E_h^{-1/4}$, and $\alpha = -3/8$. The results so obtained for the stationary structures of the ground and excited $^2A''$ states of N_3 are given in Tables 1 and 2. As seen, the barriers for pseudorotation and $N(^2D) + N_2$ reaction do not appreciably change upon CBS extrapolation. The burden of performing even more expensive ab initio calculations looks, therefore, unnecessary.

3. DMBE POTENTIAL ENERGY SURFACE

The upper (u) and lower (l) surfaces of the PES are modeled within double many-body expansion[42−45] theory as

$$V_{u/l}(R_1, R_2, R_3) = V^{(1)} + \sum_{i=1}^{3} V^{(2)}(R_i) + V_{u/l}^{(3)}(R_1, R_2, R_3) \tag{2}$$

where each n-body term is split into an extended Hartree−Fock $[V_{EHF}^{(n)}]$ and a dynamical correlation $[V_{dc}^{(n)}]$ part. Because the upper and lower surfaces of $^2A''$ symmetry dissociate to ground state N_2 and $N(^2D)$, both states will share common $V^{(1)}$ and $V^{(2)}$ terms. Similarly, the $V_{dc}^{(3)}$ term describing the long-range atom−diatom dispersion and induction energies as an inverse power series of the distance between them, assume a common form for both sheets of the DMBE PES. Following previous work on the quartet state of trinitrogen,[4] the zero energy of the PES at the atom−diatom limit will be fixed by imposing $V^{(1)} = -2D_e$, where D_e is the well depth of N_2. The specific functional forms used to describe $V^{(2)}$ and $V_{dc}^{(3)}$ can be found elsewhere.[4]

3.1. Three-Body Extended Hartree−Fock Energy. All calculated energies have been modeled via a fit to $V_{EHF}^{(3)}$ in eq 2, which is written in symmetry adapted displacement coordinates from a D_{3h} configuration of bond length R_0 as

$$\begin{pmatrix} Q_1 \\ Q_2 \\ Q_3 \end{pmatrix} = \begin{pmatrix} \sqrt{1/3} & \sqrt{1/3} & \sqrt{1/3} \\ 0 & \sqrt{1/2} & -\sqrt{1/2} \\ \sqrt{2/3} & -\sqrt{1/6} & -\sqrt{1/6} \end{pmatrix} \begin{pmatrix} R_1 - R_0 \\ R_2 - R_0 \\ R_3 - R_0 \end{pmatrix} \tag{3}$$

Table 3. Stratified Root-Mean-Square Deviations for the Two Sheets of the N_3 DMBE PES (kcal mol^{-1})

energy^a	$1^2A''$		$2^2A''$	
	N^b	rmsd	N^b	rmsd
10	11	0.158		
20	18	0.424		
30	27	0.566		
40	60	0.722		
50	103	0.784	10	0.382
60	166	0.811	20	0.668
80	359	0.838	69	1.510
100	387	0.844	141	2.009
120	424	0.934	225	2.576
140	428	0.936	257	3.143
160	432	0.933	280	3.587
180	438	0.935	289	3.602

^{a} Relative to the ground $\tilde{X}^2\Pi_g$ state. ^{b} Number of calculated ab initio points up to the indicated energy range.

The potential must then be made symmetrical with respect to permutation of the coordinates, a criterion that can be satisfied by using the integrity basis:[54,55]

$$\begin{aligned} \Gamma_1 &= Q_1 \\ \Gamma_2^2 &= Q_2^2 + Q_3^2 \\ \Gamma_3^3 &= Q_3(Q_3^2 - 3Q_2^2) \end{aligned} \tag{4}$$

Note that the functions Γ_i are totally symmetric in the three-particle permutation group S_3, and hence, any polynomial built as $P_{(m)} = \sum_{i,j,k} c_{ijk}^{(m)} \Gamma_1^i \Gamma_2^{2j} \Gamma_3^{3k}$ will also transform as the totally symmetric representation of S_3.

The nonanalytical part of the potential of H_3 has long been known to occur along the line of D_{3h} symmetry,[56,57] and so was the fact that such nonanalicity can be expressed by an additional polynomial in integer powers of the various monomers multiplied by Γ_2. In this work, we follow the same strategy as successfully applied recently[46] to the triplet state of H_3^+. This allows the fit of the adiabatic surfaces by ensuring their degeneracy along the D_{3h} line. Thus, the upper (u) and lower (l) surfaces are written as

$$\begin{aligned} V_{EHF,u}^{(3)}(\mathbf{R}) &= [P_{1,u} + \Gamma_2 P_{2,u}] \times T(\mathbf{R}) \\ V_{EHF,l}^{(3)}(\mathbf{R}) &= [P_{1,l} - \Gamma_2 P_{2,l}] \times T(\mathbf{R}) \end{aligned} \tag{5}$$

Because both Γ_2 and Γ_3 are zero at D_{3h} configurations, the only condition required to make both adiabatic sheets degenerate along the line of D_{3h} symmetry (i.e., $V_{EHF,l}^{(3)} = V_{EHF,u}^{(3)}$) is that the coefficients of the polynomials P_1, depending only on Γ_1, are kept the same, that is, $c_{i00}^{(1,l)} = c_{i00}^{(1,u)}$ for any value of i. Because eq 5 ensures that the two sheets behave as a linear function of the Jahn−Teller coordinate Γ_2 in the vicinity of the intersection seam (note that higher order terms are negligible there), the only additional constraint to impose that they have the same slope is to fix $c_{000}^{(2,l)} = c_{000}^{(2,u)}$. Finally, one may ensure that the three-body term vanishes at large interatomic distances by multiplying the polynomials in eq 5 by a
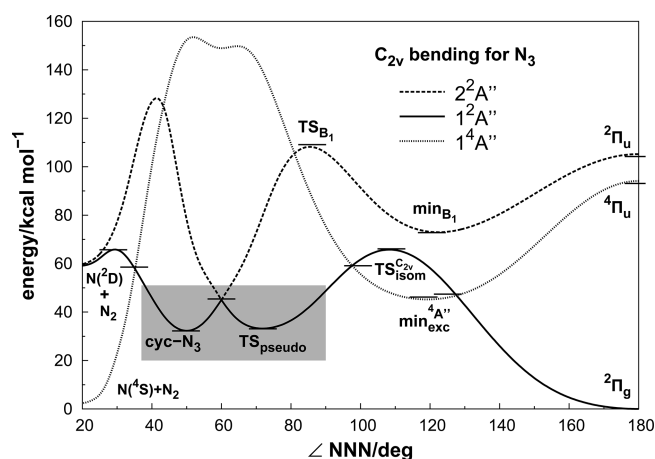
Figure 3. C_{2v} optimized energy profile for the two lowest sheets of the $^2A''$ DMBE PES, jointly with the one of $1\,^4A''$ (ref 4.). The bars show the MRCI(Q)/AVTZ prediction for the stationary structures and minima of crossing seams (ref 24). Shaded are as in Figure 1.

range-decaying term $T(\mathbf{R})$ defined as

$$T(\mathbf{R}) = \prod_{j=1}^{3}\{1 - \tanh[\gamma(R_j - R_0)]\} \qquad (6)$$

The $V_{\text{EHF},u/l}^{(3)}$ functions defined above contain 80 linear parameters $c_{ijk}^{(m)}$ each, which have been calibrated using a total of 507 ab initio points for the lower sheet and 386 for the upper one. For a better description of the stationary structures, a grid of points have been calculated at their vicinities and higher weights given to such points. As it is shown in Table 3, a good overall fit to the ab initio points has been obtained for the whole PES. Note that the ground state shows chemical accuracy over the entire range of fitted energies, while the upper one shows a somewhat larger deviation due to the presence of two other crossings with higher electronic states (see Figures 1 and 2) that were taken as avoided crossings for fitting purposes. The fitted coefficients and other relevant parameters defining both the upper and lower sheets can be found in the Supporting Information.

4. FEATURES OF THE POTENTIAL ENERGY SURFACE

Table 1 shows all known stationary structures of the lower sheet as predicted by MRCI(Q)/AVTZ optimizations[24] together with the values corresponding to the DMBE PES and the fitted form of ref 28. As shown, the DMBE PES reproduces accurately the MRCI(Q) calculations on the lower sheet, including the minima of the crossing seam (MSX) and the barriers for the $N(^2D) + N_2$ reaction. The rather complicated behavior of the upper sheet for both linear and T-shaped configurations (see Figures 1 and 2), which is due to interactions with higher electronic states, is also approximately described as avoided crossings. Note, however, that the regular stationary structures are accurately described, as shown in Table 2.

The C_{2v} bending of N_3 with optimized common bond length is shown in Figure 3 for both $^2A''$ states here studied. Also shown for completeness is the quartet state $(^4A'')$ DMBE PES previously[4] reported. To assess the accuracy of the DMBE PESs, the MRCI(Q) optimized values obtained from refs 24 and 28 are shown in this plot with line segments. As shown, all features of both doublet PESs are well described, including the location and

energetics of the spin-forbidden crossings. This is so despite the fact that the fit to the quartet state employed different ab initio methods. There are only two doublet/quartet crossings[24] that are not shown in this plot (due to their non-C_{2v} symmetry): one is of C_s symmetry lying close in energy and bond angle to the one shown at $99.3°$, the other refers to the linear dissociation of the $^2\Pi_g$ structure, which is also modeled within 1 kcal mol^{-1} by the DMBE PESs. Note that the lowest lying spin-forbidden crossing is the one shown in Figure 3, with an angle of $125°$ at 47.4 kcal mol^{-1} above the linear minima. Clearly, the stability of both isomers toward spin-forbidden or spin-allowed dissociation is well mimicked by the DMBE fits.

To allow the visualization of all stationary structures of the PES, together with all possible equivalent permutations and the connections between them, a relaxed triangular plot[58] using scaled hyperspherical coordinates, $\beta^\star = \beta/Q$ and $\gamma^\star = \gamma/Q$:

$$\begin{pmatrix} Q \\ \beta \\ \gamma \end{pmatrix} = \begin{pmatrix} 1 & 1 & 1 \\ 0 & \sqrt{3} & \sqrt{3} \\ 2 & -1 & -1 \end{pmatrix} \begin{pmatrix} R_1^2 \\ R_2^2 \\ R_3^2 \end{pmatrix} \qquad (7)$$

is employed. Note that the sum of squares of all bond distances in the triatom is relaxed such that the energy is lowest at any shape of the triangle formed by the three atoms. The lower PES is shown in Figure 4, where the stationary structures predicted by MRCI(Q) calculations and the locus of the C_{2v} symmetries are highlighted. The equilateral triangle (D_{3h}) geometry is located at the center of the plot $(\gamma^\star = \beta^\star = 0)$, which is surrounded by two sets of three equivalent minima. Closer to the center of the diagram are the minima associated to the cyc-N_3 isomers that result in a direct way from the Jahn–Teller distortion and are connected among themselves via a pseudorotation path around the conical intersection (see also refs 59–61). Note that the transition states for isomerization $TS_{\text{isom}}^{C_{2v}}$ (actually a second-order saddle point as noted above) and $TS_{\text{isom}}^{C_s}$ are correctly modeled in the DMBE PES by showing two imaginary frequencies for the former and a single one for the latter.

All barriers in the $N + N_2$ entrance channel are presented. The two transition state structures have been predicted in previous ab initio calculations:[24] one for formation of the linear minima $(TS_{\text{diss}\infty v}^{C})$, the other for the ring isomer (TS_{diss}^{C}). Although not relevant from a chemical point of view, a topological analysis shows that there is also a second-order saddle point connecting these two transition states, hereafter referred to for simplicity as $TS_{\text{diss}}^{C_s}$ and shown in Figure 4 by the symbol $\times$; for the geometrical and energetic attributes, see Table 1.

The upper sheet of the present N_3 DMBE PES is also presented as a relaxed triangular plot in Figure 5, where the three known structures $(^2\Pi_u, \text{min}_{B_1}, \text{and } TS_{B_1})$ are highlighted. Starting at min_{B_1} and following the antisymmetric stretching coordinate, one is led to another transition state that (to the best of our knowledge) has not been reported before. This transition state (TS_{C_s}) is also shown in Figure 5, connecting min_{B_1} with the dissociation to $N_2 + N(^2D)$ and has been located by CASSCF/AVTZ optimizations at a geometry of $R_1 = 2.229a_0$, $R_2 = 2.727a_0$, and $\theta = 120.7°$ with a single imaginary frequency of 1558 cm^{-1} corresponding to the antisymmetric stretch. This is predicted by the DMBE fit to lie 6.9 kcal mol^{-1} above min_{B_1}. The stability of min_{B_1} was previously[27] given to be 13.8 kcal mol^{-1} relative to the $N_2 + N(^2P)$ dissociation. If referred to the newly reported TS_{C_s}, its stability is significantly reduced.
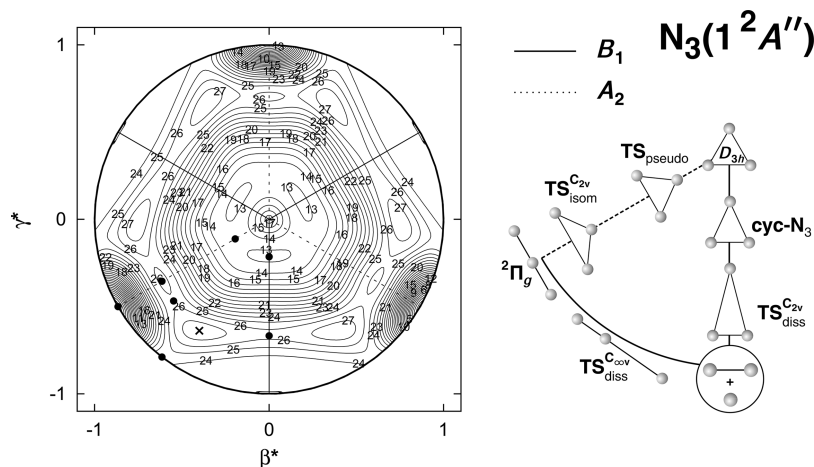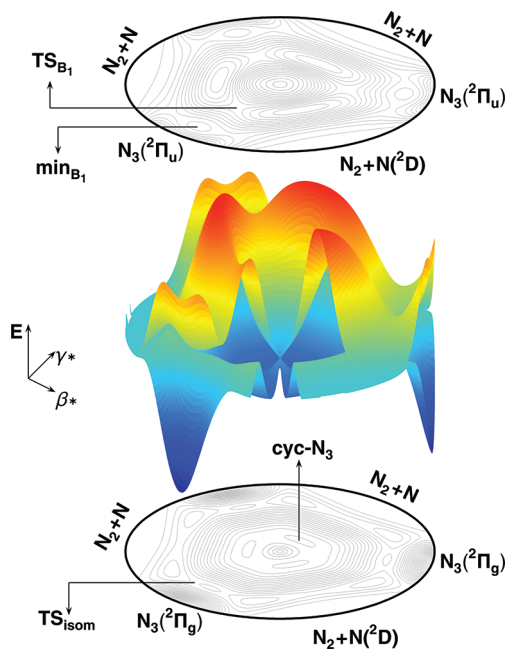
Figure 4. Relaxed triangular plot of the lower sheet of N_3 showing all its stationary structures and atomic permutations. The locus of C_{2v} geometry correlating with the $^2B_1$ electronic state is highlighted with a solid line, whereas the $^2A_2$ one is shown in dashed. Contours start at the linear minima and are spaced by 2.51 kcal mol^{-1}.
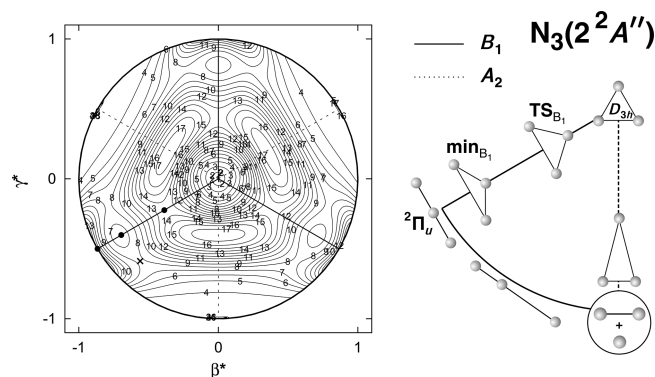
Figure 5. Relaxed triangular plot of the upper sheet of N_3 using the previous notation for the electronic states. Contours start at the minima of the crossing seam and are spaced by 5 kcal mol^{-1}.

As Figure 1 shows, the part of the upper sheet that correlates with the $^2A_2$ electronic state shows only the avoided crossing at the exit channel. Starting at TS_{B_1} (this has the imaginary frequency along the bending motion) and by following the antisymmetric stretching coordinate, it undergoes a pseudorotation that leads to the above-mentioned avoided crossing which shows two imaginary frequencies. A plot showing both surfaces together, provides a better perspective of such features and is given in Figure 6 (a cut has been made to allow visualization of the conical intersection and the well corresponding to the cyclic isomer). As this perspective view seems to suggest, the stability of min_{B_1} may not be large enough to provide a possible photoexcitation pathway for the production of cyclic N_3, as previously advanced.[27] Instead, after being brought to the $^2\Pi_u$ state, the system is likely to bend toward min_{B_1} and dissociate passing through the newly proposed TS_{C_s}, rather than overcoming the large barrier imposed by TS_{B_1}.

The isotropic (V_0) and leading anisotropic (V_2) terms in a Legendre expansion of the N_2-N interaction potential are important quantities for the study of scattering processes,[62,63] where the sign of V_2 indicates the preferred direction of the incoming atom: a negative value favors the collinear approach, while a positive value favors an attack via C_{2v} geometries. Such potentials are shown in


Figure 6. Perspective view of the two sheets of N_3 using a relaxed triangular plot.

Figure 7, where the collinear approach is shown to be preferred on the lower sheet, as expected due to the deeper well. Because the upper sheet is mostly repulsive, especially for T-shaped configurations, both components show a positive value on the short-range region. For distances larger than $7a_0$, that is, at the van der Waals interaction part of the potential, V_0 is the dominant term for both sheets, while V_2 is mostly positive, which reflects the fact that the minima of the van der Waals well lies on a T-shaped geometry, in agreement with ref 64.

5. QUASICLASSICAL STUDY OF N(^2D) + N$_2$ EXCHANGE REACTION

Due to the large masses of the atoms, quasiclassical trajectories for the N(^4S) + N$_2$ exchange reaction[5] yielded results that compared
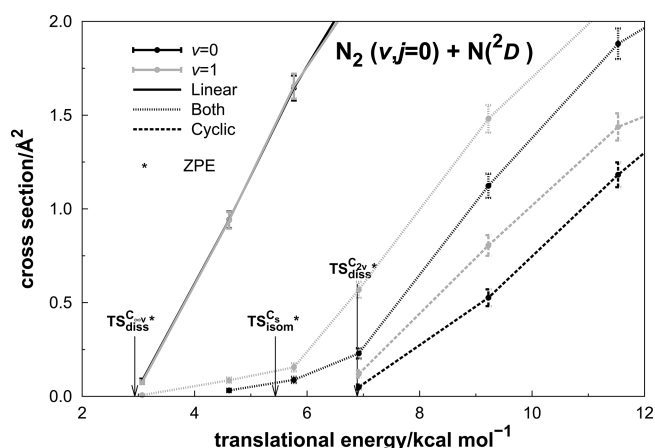
12395

dx.doi.org/10.1021/jp2073396 |*J. Phys. Chem. A* 2011, 115, 12390–12398
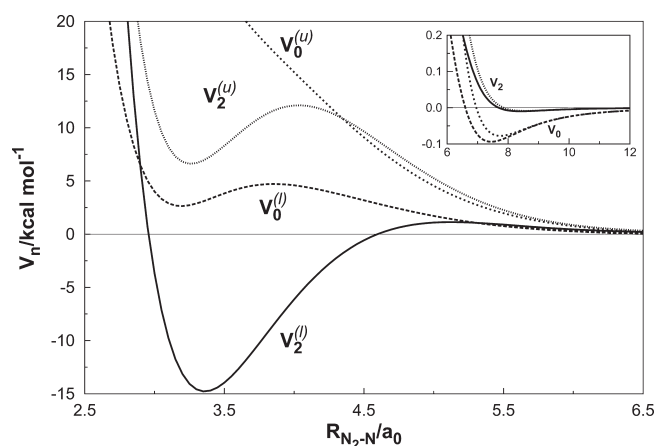
Figure 7. Isotropic (V_0) and leading anisotropic (V_2) components of the N−N$_2$ interaction potential, with the diatomic fixed at the equilibrium geometry.
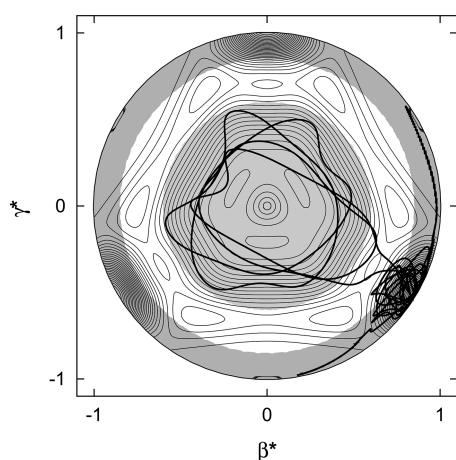
Figure 8. Trajectory path on scaled hyperspherical coordinates of eq 7, with initial translational energy of 5.8 kcal mol^{-1}. The two circles of radius 0.60 and 0.85 used to define the "linear" and "cyclic" isomeric regions are shown in gray.

Figure 9. Excitation function for formation of N$_3$ in N(^2D) and N$_2(v,j = 0)$ collisions, with separated contribution from "linear", "cyclic", and both regions of the PES. The results for $v = 0$ are shown in black, while those for $v = 1$ are shown on gray.

very well with quantum mechanical calculations,[37,38] and therefore, we use this approach to perform a first study of atom−diatom collisions also on the lowest $^2A''$ state of the system. First we have integrated trajectories[65,66] for N(^2D) + N$_2(v,j = 0)$ collisions for fixed values of the relative translational energy to obtain the excitation function. All calculations used a time step of 0.2 fs with the reactants initially separated by 17a_0, while the maximum value of the impact parameter (b_{max}) has been optimized by trial and error for each translational energy. The cross sections were then obtained as $\sigma = \pi b_{max}^2 N_r/N$, and the 68% associated errors by $\Delta\sigma = \sigma((N - N_r)/(NN_r))^{1/2}$, with N being the total number of trajectories run and N_r being the number of reactive ones.

For a study on the formation of N$_3$ from atom−diatom collisions, one must have present a third body that removes energy from the complex. Rather than attempting this (say by adding a rare gas atom), we have used the present N$_3(1^2A'')$ PES and analyzed trajectories passing through each isomer before leaving to products by counting their number and setting it as N_r. For this, we have defined two regions on the PES using geometric and energetic criteria with the scaled hyperspherical coordinates

of eq 7. A trajectory is counted as proceeding via the cyclic isomer if passing through a region inside a circle of radius 0.6 centered at $\gamma^\star = \beta^\star = 0$ and with potential energy 5 kcal mol^{-1} lower than the dissociation limit (to ensure counting only "bound" complexes). Similarly, the reaction was counted to proceed via the linear minima if it enters a region with radius larger than 0.85 and with a potential energy of 5 kcal mol^{-1} lower than the dissociation limit. The two circles defining such regions are visualized in Figure 8, which also illustrates a trajectory that passes through both isomers before forming products (with exchanged nitrogen atoms).

Figure 9 shows the excitation function for the two lowest vibrational states of N$_2$, considering trajectories that proceeded exclusively either via the linear isomer or the ring one, or passed instead through both (thus, implying trajectories that suffered isomerization before leaving to products). This graph also indicates the barriers in the PES once corrected for zero-point energy (ZPE), which should provide a threshold for each curve: TS$_{diss}^{C_{\infty v}}$ for the linear minima, TS$_{diss}^{C_{2v}}$ for the cyclic one, and TS$_{isom}^{C_s}$ for covering both minima. Although the excitation functions for the formation of only one of the isomers reasonably obey the mentioned barriers, a considerable number of trajectories with translational energies lower than TS$_{isom}^{C_s}$ were able to proceed through both linear and cyclic regions. This may be explained by ZPE leakage on the classical trajectories, because after the linear isomer is formed, the initial ZPE of N$_2(v = 0)$ that corresponds to 3.3 kcal mol^{-1} can be exchanged to promote the system on overcoming the isomerization barrier.

In a recent experiment on the formation of the azide radical from radiated solid nitrogen,[12] it was argued that the thermal energy available for collisions with N(^2D) would not be sufficient to overcome the barrier and form the linear isomer, although a quantum of vibrational excitation on the N$_2$ molecule could allow such a reaction. The QCT results reported in Figure 9 show that such a vibrational excitation is also inefficient, as would be expected from an early barrier in the context of the Polanyi rules. Indeed, vibrational to translational energy exchange would be necessary to occur before the interaction region, which is unlikely to happen. We believe that the explanation to form linear N$_3$ at low temperatures should then be that the nitrogen atom, formed from the decomposition of N$_2$, did not get thermalized and, hence, has a translational energy content larger than might

12396

dx.doi.org/10.1021/jp2073396 |*J. Phys. Chem. A* 2011, 115, 12390–12398

Table 4. Thermal Rate Constants ($10^{13}k(T)/cm^3\,s^{-1}$) for the $N(^2D) + N_2$ Atom-Exchange Reaction

| T/K | total | contributions | | |
		linear	cyclic	both
500	2.42 ± 0.14	2.23	0.00	0.19
750	8.75 ± 0.30	6.94	0.40	1.41
1000	17.92 ± 0.47	12.51	1.61	3.81

be anticipated from the temperature of the solid. Of course, the dynamics here reported is rather preliminary, because a study involving formation of the linear N_3 isomer would also require consideration of the ground $^2A'$ state (see Figure 1).

Finally, a prediction of thermal rate constants for the above atom-exchange reaction has been carried out using the PES for the $^2A''$ ground-state. For fixed temperatures, we have then sampled the relative atom—diatom translational energy and the ro-vibrational state of the N_2 molecule via cumulative distribution functions according to the QCT method.[5,65,66] The final rate constant assumes the form

$$k(T) = g_e(T)\left(\frac{8k_BT}{\pi\mu}\right)^{1/2}\sigma(T) \qquad (8)$$

where μ is the reduced mass of the reactants and $g_e(T)$ is the electronic degeneracy factor. Although the latter is usually considered to be 1/5 as its high temperature limit, we have instead used its more general form of $g_e(T) = q_{N_3}/q_{N(^2D)}q_{N_2}$, where $q_{N_2} = 1$, $q_{N_3} = 2$, and $q_{N(^2D)} = 6 + 4\exp(-12.53/T)$ is the partition function of $N(^2D)$. Table 4 gives the results of the total exchange rate constant for three temperatures ($T = 500, 750, 1000$ K), together with the specific contributions due to trajectories that "formed" only a specific isomer or both. Because this excited state of the nitrogen atom plays an important role in the atmosphere[32] (due to its reactions with O_2), and because N_2 molecules are also available in large abundances, this reaction may be relevant for the study of atmospheric chemistry, although the formation of a stable N_3 molecule is very unlikely under such conditions and, even if formed, should be quickly decomposed by reactions with other reactive species.

6. CONCLUDING REMARKS

We have reported a global representation of the two lowest $^2A''$ states of the azide radical using DMBE theory and MRCI-(Q)/AVTZ calculations for the calibration procedure. To our knowledge, this is the only available PES suitable for scattering calculations because it describes all dissociation channels. Moreover, it accurately reproduces all stationary structures predicted for the lower and upper adiabatic sheets. A preliminary QCT study on the dynamics of this system on the lowest sheet of the potential energy surface has also been reported, with the contribution of each isomer pathway being investigated during the collisional process.

ASSOCIATED CONTENT

S **Supporting Information.** All coefficients necessary to construct the potential energy surfaces reported in this work are available in four tables. This material is available free of charge via the Internet at http://pubs.acs.org.

AUTHOR INFORMATION

Corresponding Author
*E-mail: varandas@qtvs1.qui.uc.pt.

ACKNOWLEDGMENT

REFERENCES

(1) Samartzis, P. C.; Wodtke, A. M. *Int. Rev. Phys. Chem.* **2006**, *25*, 572.

(2) Zarko, V. E. *Combust., Explos., Shock Waves* **2010**, *46*, 121.

(3) Bittererová, M.; Östmark, H.; Brinck, T. *J. Chem. Phys.* **2002**, *116*, 9740.

(4) Galvão, B. R. L.; Varandas, A. J. C. *J. Phys. Chem. A* **2009**, *113*, 14424.

(5) Caridade, P. J. S. B.; Galvão, B. R. L.; Varandas, A. J. C. *J. Phys. Chem. A* **2010**, *114*, 6063.

(6) Tian, R.; Facelli, J. C.; Michl, J. *J. Chem. Phys.* **1988**, *92*, 4073.

(7) Tian, R.; Michl, J. *Faraday Discuss., Chem. Soc.* **1988**, *86*, 113.

(8) Hassanzadeh, P.; Andrews, L. *J. Phys. Chem.* **1992**, *96*, 9177.

(9) Khabasheskua, V. N.; Margrave, J. L.; Waters, K.; Schultz, J. A. *J. Appl. Phys.* **1997**, *82*, 1921.

(10) Sankaran, K.; Sundararajan, K.; Viswanathan, K. S. *J. Phys. Chem. A* **2001**, *105*, 3995.

(11) Hudson, R. L.; Moore, M. H. *Astrophys. J.* **2002**, *568*, 1095.

(12) Amicangelo, J. C.; Collier, J. R.; Dine, C. T.; Saxton, N. L.; Schleicher, R. M. *Mol. Phys.* **2007**, *105*, 989.

(13) Jamieson, C. S.; Kaiser, R. I. *Chem. Phys. Lett.* **2007**, *440*, 98.

(14) Brazier, C. R.; Bernath, P. F.; Burkholder, J. B.; Howard, C. J. *J. Chem. Phys.* **1988**, *89*, 1762.

(15) Douglas, A. E.; Jones, W. J. *Can. J. Phys.* **1965**, *43*, 2216.

(16) Thrush, B. A. *Proc. R. Soc., A* **1956**, *235*, 143.

(17) Martin, J. M. L.; François, J. P.; Gijbels, R. *J. Chem. Phys.* **1989**, *90*, 6469.

(18) Hansen, N.; Wodtke, A. M. *J. Phys. Chem. A* **2003**, *107*, 10608.

(19) Samartzis, P. C.; J. J.-M. Lin, T.-T. C.; Chaudhuri, C.; Lee, Y. T.; Lee, S.-H.; Wodtke, A. M. *J. Chem. Phys.* **2005**, *123*, 051101.

(20) Zhang, J.; Zhang, P.; Chen, Y.; Yuan, K.; Harich, S. A.; Wang, X.; Wang, Z.; Yang, X.; Morokuma, K.; Wodtke, A. M. *Phys. Chem. Chem. Phys.* **2006**, *8*, 1690.

(21) Samartzis, P. C.; J. J.-M. Lin, T.-T. C.; Chaudhuri, C.; Lee, S.-H.; Wodtke, A. M. *J. Chem. Phys.* **2007**, *126*, 041101.

(22) Samartzis, P. C.; Wodtke, A. M. *Phys. Chem. Chem. Phys.* **2007**, *9*, 3054.

(23) Larson, C.; Ji, Y.; Samartzis, P. C.; Quinto-Hernandez, A.; Lin, J. J.; Ching, T.-T.; Chaudhuri, C.; Lee, S.-H.; Wodtke, A. M. *J. Phys. Chem. A* **2008**, *112*, 1105.

(24) Zhang, P.; Morokuma, K.; Wodtke, A. M. *J. Chem. Phys.* **2005**, *112*, 014106.

(25) Yu, X.-F.; Jin, L.; Ding, Y.-H. *J. Mol. Struct.: THEOCHEM* **2009**, *911*, 13.

(26) Jin, L.; Yu, X.-F.; Pang, J.-L.; Zhang, S.-W.; Ding, Y.-H. *J. Phys. Chem. A* **2009**, *113*, 8500.

(27) Kerkines, I. S. K.; Wang, Z.; Zhang, P.; Morokuma, K. *Mol. Phys.* **2009**, *107*, 1017.

(28) Wang, Z.; Kerkines, I. S. K.; Morokuma, K.; Zhang, P. *J. Chem. Phys.* **2009**, *130*, 044313.

(29) Murrell, J. N.; Novaro, O.; Castillo, S. *Chem. Phys. Lett.* **1982**, *90*, 421.

(30) Wasilewski, J. *J. Chem. Phys.* **1996**, *105*, 10969.

(31) Continetti, R. E.; Cyr, D. R.; Osborn, D. L.; Leahy, D. J.; Neumark, D. M. *J. Chem. Phys.* **1993**, *99*, 2616.

(32) Tohmatsu, T. *Compendium of Aeronomy*; Kluwer Academy: Norwell, MA, 1990.

(33) Kunsch, P. L.; Dressler, K. *J. Chem. Phys.* **1978**, *68*, 2550.

(34) Kunsch, P. L. *J. Chem. Phys.* **1978**, *68*, 4564.

(35) Oehler, O.; Smith, D. A.; Dressler, K. *J. Chem. Phys.* **1977**, *66*, 2097.

(36) Kajihara, H.; Okada, F.; Koda, S. *Chem. Phys.* **1994**, *186*, 395.

(37) Wang, D.; Stallcop, J. R.; Huo, W. M.; Dateo, C. E.; Schwenke, D. W.; Partridge, H. *J. Chem. Phys.* **2003**, *118*, 2186.

(38) Garcia, E.; Saracibar, A.; Gomez-Carrasco, S.; Laganá, A. *J. Phys. Chem. A* **2008**, *10*, 2552.

(39) Babikov, D.; Zhang, P.; Morokuma, K. *J. Chem. Phys.* **2004**, *121*, 6743.

(40) Babikov, D.; Kendrick, B. K.; Zhang, P.; Morokuma, K. *J. Chem. Phys.* **2005**, *122*, 044315.

(41) Babikov, D.; Kendrick, B. K. *J. Chem. Phys.* **2010**, *133*, 174310.

(42) Varandas, A. J. C. *J. Mol. Struct.: THEOCHEM* **1985**, *21*, 401.

(43) Varandas, A. J. C. *Adv. Chem. Phys.* **1988**, *74*, 255–337.

(44) Varandas, A. J. C. In *Lecture Notes in Chemistry*; Laganá, A., Riganelli, A., Eds.; Springer: Berlin, 2000; Vol. 75, pp 33–56.

(45) Varandas, A. J. C.; *Advanced Series in Physical Chemistry*; World Scientific Publishing: Hackensack, NJ, 2004; Chapter 5, p 91.

(46) Varandas, A. J. C.; Alijah, A.; Cernei, M. *Chem. Phys.* **2005**, *308*, 285–295.

(47) Werner, H. J.; Knowles, P. J. *J. Chem. Phys.* **1988**, *89*, 5803.

(48) Knowles, P. J.; Werner, H. J. *Chem. Phys. Lett.* **1988**, *145*, 514.

(49) Werner, H.-J.; Knowles, P. J.; Lindh, R.; Manby, F. R.; Schütz, M.; Celani, P.; Korona, T.; Mitrushenkov, A.; Rauhut, G.; Adler, T. B.; Amos, R. D.; Bernhardsson, A.; Berning, A.; Cooper, D. L.; Deegan, M. J. O.; Dobbyn, A. J.; Eckert, F.; Goll, E.; Hampel, C.; Hetzer, G.; Hrenar, T.; Knizia, G.; Köppl, C.; Liu, Y.; Lloyd, A. W.; Mata, R. A.; May, A. J.; McNicholas, S. J.; Meyer, W.; Mura, M. E.; Nicklass, A.; Palmieri, P.; Pflüger, K.; Pitzer, R.; Reiher, M.; Schumann, U.; Stoll, H.; Stone, A. J.; Tarroni, R.; Thorsteinsson, T.; Wang, M.; Wolf, A. *Molpro*, version 2008.3, a package of ab initio programs; 2008.

(50) Dunning, T. H., Jr. *J. Chem. Phys.* **1989**, *90*, 1007.

(51) Kendall, R. A.; Dunning, T. H., Jr.; Harrison, R. J. *J. Chem. Phys.* **1992**, *96*, 6796.

(52) Karton, A.; Martin, J. M. L. *Theor. Chem. Acc.* **2006**, *115*, 330–333.

(53) Varandas, A. J. C. *J. Chem. Phys.* **2007**, *126*, 244105.

(54) Weyl, H. *The Classical Theory of Groups*; Princeton University Press: Princeton, NJ, 1946.

(55) Murrell, J. N.; Carter, S.; Farantos, S. C.; Huxley, P.; Varandas, A. J. C. *Molecular Potential Energy Functions*; Wiley: Chichester, 1984.

(56) Varandas, A. J. C.; Murrell, J. N. *Faraday Discuss., Chem. Soc.* **1977**, *62*, 92–109.

(57) Porter, R. N.; Stevens, R. M.; Karplus, M. *J. Chem. Phys.* **1968**, *49*, 5163.

(58) Varandas, A. J. C. *Chem. Phys. Lett.* **1987**, *138*, 455.

(59) Babikov, D.; Mozhayskiy, V. A.; Krylov, A. I. *J. Chem. Phys.* **2006**, *125*, 084306.

(60) Mozhayskiy, V. A.; Babikov, D.; Krylov, A. I. *J. Chem. Phys.* **2006**, *124*, 224309.

(61) Babikov, D. *J. Chem. Phys.* **2011**, *134*, 114305.

(62) Norbeck, J. M.; Certain, P. R.; Tang, K. T. *J. Chem. Phys.* **1975**, *63*, 590.

(63) Varandas, A. J. C. *J. Chem. Phys.* **1979**, *70*, 3786.

(64) Stallcop, J. R.; Partridge, H. *Phys. Rev. A* **2001**, *64*, 042722.

(65) Peslherbe, G. H.; Wang, H.; Hase, W. L. *Adv. Chem. Phys.* **1999**, *105*, 171.

(66) Hase, W. L.; Duchovic, R. J.; Hu, X.; Komornik, A.; Lim, K. F.; Lu, D.-H.; Peslherbe, G. H.; Swamy, K. N.; van de Linde, S. R.; Varandas, A. J. C.; Wang, H.; Wolf, R. J. *QCPE Bull.* **1996**, *16*, 43.